説明文書（健常人ボランティア用）

研究課題名

走査型蛍光X線顕微鏡を用いた血液疾患患者血液・骨髄細胞における
細胞内元素変動解析

1．はじめに（本研究の意義及び目的）

血液疾患の多くは、その発症メカニズムが十分に解明されておらず、有用な診断法、また有効な治療法についての研究開発が必要です。本研究は、走査型蛍光X線顕微鏡(注)という新しい技術を用いて、血液細胞や骨髄細胞のミネラル（元素）変動を調べるものです。ミネラル（元素）は、細胞代謝に必須であり、バランスを損なうと体調に変化が出ることも知られています。最近、このミネラルが、腫瘍細胞などの特徴と密接に関連していることが徐々にわかってきました。この研究により、今までわからなかった血液疾患の血液細胞や骨髄細胞のミネラル変動を詳しく調べることができます。この研究により新しい診断法や治療法の開発の助けになる可能性があります。

これからご説明することをご理解いただいた上で、この新しい技術を用いた研究のために、末梢血液を提供して頂きたく御協力をお願い致します。

（注）走査型蛍光X線顕微鏡とは？

生体内では、適切な量の鉄、銅、カルシウム、マグネシウム、カリウム等ミネラル（元素）は代謝に必須な成分であることが知られています。この顕微鏡では、被写体（細胞）の生体内の大旨全てのミネラル（元素）を観ることができます．また、生体内では様々な細胞が存在し、それぞれ役割分担があります．近年、細胞は外界の刺激に対して、細胞のミネラル（元素）に変動を起こすことを、この顕微鏡を用いて世界で初めて観ることができるようになりました．現在、日本はこの分野において世界最高水準にあります．

2．研究協力は任意であり、撤回も自由であること

この研究への協力への同意はあなたの自由意志で決めて下さい。一旦同意した場合でも、あなたが不利益を受けることなく、いつでも同意を取り消すことができ、その場合は採取した試料（末梢血液）や調べた結果などは廃棄され、診療記録などもそれ以降は研究目的に用いられることはありません。

3．研究のあらまし

研究名：走査型蛍光X線顕微鏡を用いた血液疾患患者血液・骨髄細胞における元素分析
研究の目的：血液疾患患者の末梢血液および骨髄細胞について走査型蛍光X線顕微鏡を用いて、細胞内の様々な元素分析を行い、血液疾患患者血液・骨髄細胞に特徴的な元素の変動を調べます。また健常人ボランティアを募り血液中の元素を比較します。

研究機関名及び研究者・研究責任者氏名：

研究責任者

所属機関		職名	氏名
国立国際医療センター病院	血液内科	5階北病棟医長	萩原將太郎

共同研究者

国立国際医療センター病院	血液内科	第1内科医長	三輪哲義
国立国際医療センター研究所	難治性疾患研究部部長		石坂幸人
	難治性疾患研究部難治性疾患研究室		志村まり

研究の方法：

末梢血液約１０ｍｌをいただきます。提供していただいた末梢血液から血漿あるいは血液細胞を分離し、走査型蛍光Ｘ線顕微鏡という特殊な装置をもちいて、細胞の中に含まれる元素を測定します。また ICP-MS という装置を用いて血液中の元素を測定します。特定の元素が患者検体と比較して変動が見出される場合には、血液細胞・血漿に含まれる元素に結びついている蛋白質を解析します。

４．予測される結果、研究協力者にもたらされる利益および不利益について

この研究は、血液疾患の患者さんの協力を得て、血液疾患の血液および骨髄における元素を調べるものです。研究の結果から、将来の血液疾患の患者さんにとって役に立つ情報が得られる可能性がありますが、あなたへの直接的な利益はありません。

５．個人情報が第三者から保護され、匿名化され、研究成果が公表されること

個人名につきましては当センターの個人情報識別管理者**（研究代表者）**が番号で置き換えてわからないようにしてから、年齢、性別、検査所見などに関係するデータのみを添付して研究に使わせていただきます。研究の結果は、学会や学術雑誌等に発表しますが、その場合もプライバシーは保護されます。

あなたの協力によって得られた研究の成果を学会発表や学術雑誌およびデータベース上等で公表する際にはあなたの個人名を匿名とし、あなたが特定されるような状況はないように配慮されます。

本研究では、あなたの**末梢血液に**含まれる元素や元素似結びついている蛋白を調べますが、遺伝情報についての解析は行いません。測定後の検体**（末梢血液）**は適切な方法（オートクレーブ＝高熱処理）により廃棄されます。

あなたの検体**（末梢血液）**は、研究に用いられる前に氏名などの個人情報が取り除かれ、本研究の研究代表者によって新たに番号が付されます。これを試料の匿名化といいます。本研究ではこのように匿名化された試料を用いることで、あなたのプライバシーが保護された状態で解析を行います。また本研究計画の結果を論文として公表する際にも個人の特定化が可能になるようにはいたしません。

６．研究から生じるかもしれない知的財産権は研究協力者（あなた）には属さないこと

解析研究の結果として特許権などが生じる場合でも、残念ですが、試料を提供して下さった方のものにはなりません。あなたから提供していただいた試料を用いた研究によって、疾患の診断や治療に役立つような情報が発見され特許権などが生じることも考えられます。この様な知的所有権は研究者又は研究者の所属する施設に帰属し、試料を提供して下

さったあなたには帰属しないことになります。何卒ご了解下さい。

7．研究協力は無償で行われ、研究協力者に費用の負担はないこと

検体の提供は無償でお願いいたします。もちろん研究協力者の方に費用の御負担はありません。

平成　　年　　月　　日

お問い合わせ先
国立国際医療センター血液内科　５階北病棟医長
萩原將太郎

〒162-8655 東京都新宿区戸山 1-21-1
TEL 03-3202-7181（代表）
FAX 03-3207-1038（代表）

研究協力についての同意書（健常ボランティア用）

申請番号（　　）

国立国際医療センター総長殿

私は、走査型蛍光 X 線顕微鏡を用いた血液疾患患者における元素分析について、下記説明者より説明文書を用いて以下の項目の説明を受けました。

・研究協力は任意であり、撤回も自由であること
・研究の意義、目的と方法
・研究から生じるかもしれない知的財産権は研究協力者に属さないこと
・研究終了後の試料等の取り扱い方法
・研究は無償に行われ、研究協力者に費用の負担はないこと

特に、以下の項目に関しては了解したことを□にチェックし、確認いたします。

□末梢血液を提供していただくこと
□研究協力者にもたらされる利益および不利益について
□個人情報は第三者に漏れることなく、匿名化された上で研究成果が公表されること
□**末梢血液の解析**が終了した後は直ちに試料は廃棄されること

以上より、私は上記の研究に協力することに（下記を○で囲んで下さい）

同意します　　同意しません

平成　　年　　月　　日

研究協力者氏名（署名または記名、捺印）

説明者の職名、氏名（署名または記名、捺印）

研究成果の刊行に関する一覧表

雑誌

発表者氏名	論文タイトル名	発表誌名	巻号	ページ	出版年
Nishino Y. et al.	Three-Dimensional Visualization of a Human Chromosome Using Coherent X-ray Diffraction	Physical Review Letters	102	18101-18104	2009
Matsuyama S., et al.	Trace element mapping of a single cell using a hard x-ray nanobeam focused by a Kirkpatrick-Baez mirror system	X-ray Spectrometry	38	89-94	2009
Matsuyama S., et al.	Trace element mapping using a high-resolution scanning X-ray fluorescence microscope equipped with a Kirkpatrick-Baez mirror system	Surf. Interface Anal.	40	1042-1045	2008
Eltsov M. et al.	Analysis of cryo-electron microscopy images does not support the existence of 30-nm chromatin fibers in mitotic chromosomes in situ.	Proc. Natl. Acad. Sci. USA.	105	19732-19737	2008
Yamagishi Y, et al	Heterochromatin links to centromeric protection by recruiting shugoshin.	Nature	455	251-255	2008

Three-Dimensional Visualization of a Human Chromosome Using Coherent X-Ray Diffraction

Yoshinori Nishino,[1,*] Yukio Takahashi,[2] Naoko Imamoto,[3] Tetsuya Ishikawa,[1] and Kazuhiro Maeshima[3]

[1]*RIKEN SPring-8 Center, 1-1-1 Kouto, Sayo-cho, Sayo-gun, Hyogo 679-5148, Japan*

[2]*Graduate School of Engineering, Osaka University, 2-1 Yamada-oka, Suita, Osaka 565-0871, Japan*

[3]*Cellular Dynamics Laboratory, RIKEN, 2-1 Hirosawa, Wako, Saitama 351-0198, Japan*

(Received 10 July 2008; revised manuscript received 18 November 2008; published 5 January 2009)

Coherent x-ray diffraction microscopy is a lensless phase-contrast imaging technique with high image contrast. Although electron tomography allows intensive study of the three-dimensional structure of cellular organelles, it has inherent difficulty with thick objects. X rays have the unique benefit of allowing noninvasive analysis of thicker objects and high spatial resolution. We observed an unstained human chromosome using coherent x-ray diffraction. The reconstructed images in two or three dimensions show an axial structure, which has not been observed under unstained conditions.

DOI: 10.1103/PhysRevLett.102.018101 PACS numbers: 87.59.−e, 42.30.Wb, 61.05.cp, 87.16.Sr

Mesoscopic-scale structures, such as higher-order structures in cellular organelles, play a key role in elucidating the connection between macroscopic properties and atomic structures, but are often too thick to observe under a transmission electron microscope [1,2]. X rays can be used to observe internal mesoscopic structures owing to their short wavelength and high penetrating power [3–6].

Coherent x-ray diffraction occurs when a sample is illuminated by x rays with a well-defined wave front, and its high sensitivity to the sample structure can be utilized for microscopy [7–9]. The coherent diffraction pattern is speckled when the sample is disordered. In an experiment, the speckled diffraction pattern has to be sampled finely enough to satisfy the oversampling condition, which is derived from the Shannon sampling theorem, as Sayre originally pointed out in 1952 [7]. The coherently diffracted wave is related to the sample electron-density map by Fourier transform, but the phase of the diffracted wave is not directly measurable. In x-ray diffraction microscopy, a sample image is reconstructed by retrieving the phase using an iterative method [10]. Coherent diffraction in the hard x-ray regime can provide three-dimensional (3D) electron-density maps, a seamless connection with x-ray crystallography. Despite strong interest in biological applications, biological studies have been limited to two-dimensional (2D) observations [11–14]. We report for the first time 3D electron-density mapping of an uncrystallized biological sample using coherent x-ray diffraction.

Coherent x-ray diffraction microscopy is an ideal form of x-ray phase-contrast imaging, since there is no contrast degradation due to lenses. Meanwhile, conventional soft x-ray zone plate microscopes and x-ray contact microscopes provide absorption contrast [3–5]. As is well recognized in optical microscopy, phase-contrast imaging generally offers better image contrast than absorption contrast imaging for transparent objects, such as unstained biological specimens. In the x-ray regime also, it has been reported that lower radiation dose and higher image contrast can be achieved with phase-contrast imaging compared to absorption contrast imaging, even in the water window region [15]. The reconstructed images of an unstained human chromosome shown in this Letter have axial structure, which other microscopic methods have been unable to visualize under unstained conditions, and the result experimentally demonstrates the high imaging ability of coherent x-ray diffraction for unstained biological specimens.

Chromosomes are essential organelles for the faithful transmission of duplicated genomic DNA into two daughter cells during cell division [16,17]. Although more than 100 years have passed since chromosomes were first observed, how a long string of genomic DNA is packaged into compact chromosomes remains unclear. Since whole-mount chromosomes are too thick for electrons, thin-sectioning is unavoidable in transmission electron microscopy; however, it generally requires sample preparation and often causes deformation of the sections [1]. Although light microscopy with immunofluorescence or fluorescent proteins can image whole-mount chromosomes, the distribution of specific proteins only can be observed, requiring *a priori* knowledge or conjecture about the sample. Therefore, x rays have a unique potential for analyzing the entire structure of whole-mount chromosomes.

We purified individual chromosomes from mitotic HeLa cells as described previously [18]. The chromosomes were fixed chemically in a compact form with a buffer including 10 mM Hepes-KOH, 5 mM $MgCl_2$ and 0.5% glutaraldehyde for 10 min. The fixed chromosomes were spread over a 100-nm-thick silicon nitride membrane by gentle centrifugation to adhere the chromosomes to the membrane at an appropriate density. The chemically fixed chromosomes on the silicon nitride membrane were washed once with pure distilled water to remove salt and then allowed to dry in air.

We observed a human chromosome sample under our coherent x-ray diffraction microscope using the BL29XUL hard x-ray undulator beam line at SPring-8. Figure 1 shows the experimental setup schematically. X rays at an energy of 5 keV pass through a 20-μm-diameter pinhole to illu-

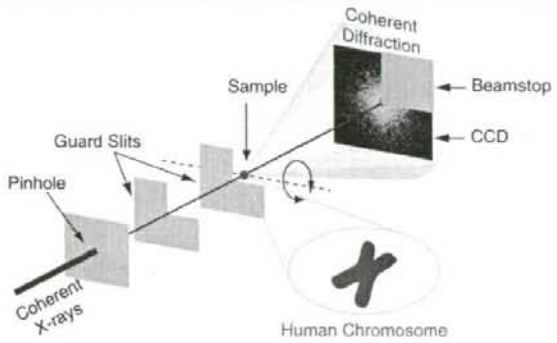

FIG. 1 (color). Schematic view of coherent hard x-ray diffraction measurement of an unstained human chromosome. A 20-μm-diameter pinhole ~1 m upstream from the sample defined the illumination for a single chromosome. Two guard slits were aligned carefully to reduce the amount of missing data near forward-scattering angles. An x-ray CCD detector 1.32 m downstream from the sample was used to acquire coherent diffraction data. The CCD has a pixel size of 20 μm, and an imaging array of 1340 × 1300 pixels. A beam stop 365 mm upstream from the CCD blocked the unscattered direct x-ray beam, and shaded nearly a quadrant area of the CCD. The centrosymmetry of the diffraction data was used to recover some of the missing data behind the beam stop. The sample was rotated for 3D image reconstruction.

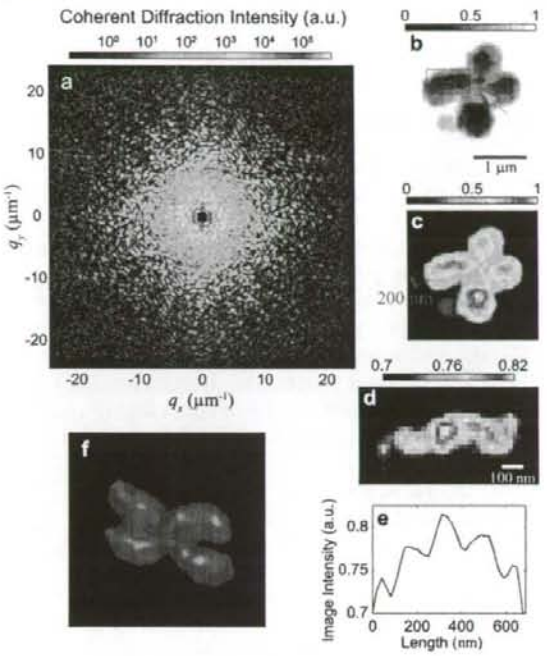

FIG. 2 (color). Coherent diffraction pattern of an unstained human chromosome and its reconstructed projection image. The reconstruction of coherent x-ray diffraction data (a) gave a chromosome image [(b) in gray scale and (c) in color scale]. The centromere region is indicated by an arrow in (b). The reconstructed image contains a high-intensity region resembling the chromosome axial structure near the center of the chromatids, as clearly shown in (c). (d) shows an enlarged image of the region in the red square in (b), where a different color scale was used to enhance the structure. A wavy feature in (d) is similar to the helical axis structure observed in the immunofluorescence imaging [18]. The wavy structure is also evident in the profile (e) along the magenta line in (b). (f) shows an immunofluorescence image of a different chromosome, stained by a condensin antibody (red) and DAPI (blue), showing a wavy axial structure (red). $\boldsymbol{q}$ is defined as $|\boldsymbol{q}| = 2\sin(\Theta/2)/\lambda$, where Θ is the scattering angle.

minate the target chromosome only. The photon flux after the pinhole was $\sim 1 \times 10^{10}$ photons/s. The beam size at the sample (the size of the first robe of the pinhole diffraction) is calculated to be 33 μm. Our measurement is insensitive to the positional drift of the sample, because the illuminating beam size is an order of magnitude larger than the sample size, and there is no neighboring object near the sample chromosome. The coherent diffraction from the sample is recorded with an x-ray direct-detection charge-coupled device (CCD). In the data analysis, we used 800 × 800 pixel data, which provided reconstructed images with a single pixel (or a voxel) size of 20.5 nm in each dimension. For 3D reconstruction, we measured data at different incident angles ranging from $-70°$ to $+70°$ at intervals of 2.5° or 5°. In the data analysis, we excluded data at some angles suffering from strong background scattering. The exposure time at each incident angle was 2700 s for the sample data (except for the data shown in Fig. 2, which had a 3400 s exposure) and half of that for the background data. The radiation dose was 4×10^8 Gy for a single incident angle and 2×10^{10} Gy for full 3D data acquisition.

Our coherent diffraction measurement produced high-contrast speckle patterns, as shown in Fig. 2(a), though the sample human chromosome was not stained. Speckles in the coherent diffraction patterns have a typical size of ~8 pixels on the detector in each dimension; therefore, our measurement safely satisfies the oversampling condition. We achieved a typical missing data size of 23 pixels near the diffraction center.

We reconstructed an image from the coherent diffraction data by applying an iterative phasing method [10,19,20]. Specifically, we used the HIO algorithm [10] with the iterative normalization [19]. The iterative process started from a random electron-density map in a rectangular support (99 × 98 pixels), and the support was revised iteratively [20] every 500 iterations using intermediately reconstructed images. Here, the support is the area where the sample is supposed to exist. In the iterative process, the electron density outside the support is forced to decrease gradually in real space, and the measured coherent diffraction data is used in reciprocal space. The iterative process

continued for up to 2×10^4 iterations. Images were reconstructed starting from 15 different random electron-density maps, and the ten most similar resultant images were averaged after careful alignment to achieve the final reconstruction. The similarity evaluation and the alignment were performed numerically by comparing digital images.

A 2D reconstruction of the human chromosome is shown in gray scale [Fig. 2(b)] and in color scale [Fig. 2(c)]. In these figures, the image intensities are proportional to the projection of the electron density in the direction of the incident x-ray beam. According to our estimation using the phase retrieval transfer function [21], the spatial resolution (half-period resolution) of the 2D reconstruction is 38 nm. This implies that the Fourier transform of the reconstructed image is highly consistent with the measured coherent diffraction data below the resolution frequency.

The 2D projection image [Figs. 2(b) and 2(c)] clearly shows a pair of sister chromatids attached to each other at the centromere region [indicated by an arrow in Fig. 2(b)]. We even observed a protrusion from the bottom arm of the chromosome in lower image intensities; this is likely part of another chromosome that failed to separate during sample preparation. The most striking feature in the 2D reconstruction is the high image-intensity region near the center of the chromatids, which is obvious in the color scale image [Fig. 2(c)]. The high image-intensity region has a width of ~200 nm, and the intensity is typically ~1.5 times greater than in the other region. This region roughly coincides with where the so-called chromosome scaffold or axis appears. The axis was reported to consist of condensin and topoisomerase IIα, which are essential proteins for the chromosome assembly process [16–18]. The axial structure has so far been detected only using immunoelectron microscopy or fluorescence microscopy on labeling its components, which have a diameter of ~200 nm at the center of each chromatid in isolated chromosomes and even in chromosomes in living cells [16,17]. The corresponding region in our reconstruction has a wavy structure, as shown in the enlarged image in Fig. 2(d). This wavy feature is similar to the helical structure in the chromosome, as observed with immunofluorescence imaging [18], but has not been seen in unstained chromosomes. Figure 2(f) shows an immunofluorescence imaging of a different chromosome, showing an axial structure (red) in the chromosome body (blue).

A greater image intensity in 2D projection images implies a greater electron density or a thicker sample depth, and a 3D reconstruction allows us further interpretation. For 3D data analysis, we used coherent diffraction data sets at 38 incident angles, and performed image reconstruction in a similar way as in the 2D case but using 3D Fourier transformation. The diffraction intensity in each voxel was obtained from the measured coherent diffraction data sets by interpolation [22]. Prior to the interpolation, each diffraction data set was normalized using the total number of electrons in the 2D reconstruction at each incident angle. The iterative process continued for up to 1×10^4 iterations for the 3D case, and the final averaging process was applied as in the 2D case.

Figure 3 shows our 3D reconstruction. It shows not only the surface morphology [Fig. 3(a)], but also the internal electron-density map [Figs. 3(b), 3(c), and 3(e)]. Interestingly, we found the greatest electron density around the centromere (indicated by arrows). Figures 3(b) and 3(c) show cross-sectional images through the highest density position in the horizontal and vertical planes, respectively. Our observation can be explained by the fact that the centromere region is composed entirely of constitutive heterochromatin and is more condensed than other chromosomal regions. In the projection image [Fig. 3(d)] generated from the 3D reconstruction, the greatest image intensity appears at the bottom arm of the chromosome which is consistent with our 2D reconstruction [Figs. 2(b) and 2(c)].

Near the central axis of each chromatid, the electron density is also relatively high [Figs. 3(b), 3(c), and 3(e)]. This result indicates that the axial region has a greater electron density than the average, at least in this sample, and again suggests the region is more condensed. The wavy structure observed in the 2D reconstruction was not recognized in the 3D case, since the spatial resolution was

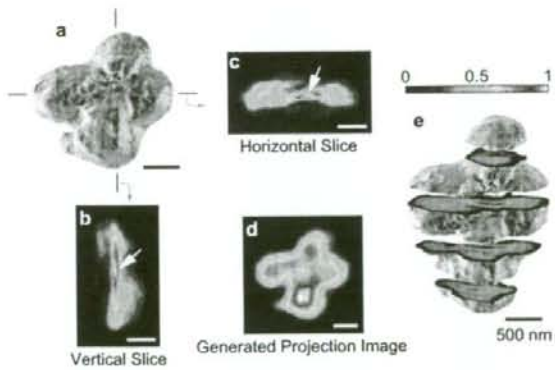

FIG. 3 (color). Reconstructed 3D electron-density map of an unstained human chromosome. The isosurface (a) of the chromosome was drawn with a threshold value at 15% of the highest density. The planes of the cross-sectional images (b,c) include the position near the centromere (indicated by arrows) with the highest electron density. They show relatively high density near the central axis of each chromatid. The projection image (d) generated from the 3D reconstruction has a similar feature to that in the 2D reconstruction in Figs. 2(b) and 2(c). (e) shows cross-sectional images of the chromosome at 409 nm intervals. The diffraction data sets used for the 3D analysis are at 38 incident angles: every 2.5° from −70° to −27.5°, as well as −7.5°, −5°, 0°, 5°, 7.5°, 10°, 15°, 17.5°, 20°, 25°, 27.5°, 30°, 37.5°, 40°, 45°, 47.5°, 50°, 55°, 57.5°, and 60°.

lower. We estimate the spatial resolution of the 3D reconstruction to be 120 nm from the phase retrieval transfer function [21]. Nevertheless, this is amongst the highest resolutions ever achieved for 3D x-ray phase-contrast imaging [23,24]. The result also implies that our microscope detects the phase shift of x-ray waves with great sensitivity. Judging from the radiation dose of our measurement, 2×10^{10} Gy, and the reported feature-destroying dose [25,26], the resolution degradation in the 3D case is caused primarily by radiation damage. For organic samples, mass loss due to outgassing occurs after radiation-induced bond braking, and causes morphological change [3]. Higher resolution is expected to be achieved by carefully optimizing the radiation dose in consideration of the dose fractionation theorem [27] and by cryogenically cooling the sample. Note that we succeeded in reconstructing 3D images, even when radiation damage presumably develops over the measurement time. A similar phenomenon would also be seen in any tomographic imaging.

Our findings give clear guidelines for the 3D structure analysis of thick unstained biological samples using hard x rays, and our method was shown to provide structural information that complements conventional imaging methods experimentally. This was realized as a consequence of our high-quality data acquisition of coherent diffraction. Our method eliminates the shortcomings of hard x-ray microscopy using lenses, realizing an ideal form of lensless phase-contrast hard x-ray imaging. As Henderson discussed after considering the electron mean free path, x rays can offer a superior performance compared to the electrons for biological samples thicker than ~500 nm [2]. Since our sample was dried, measurement in a hydrated state is the ultimate goal for observing samples closer to their natural state. In the measurement of frozen-hydrated biological samples, where vitreous ice is widely spread, coherent diffraction measurement with scanning of the finite illumination area (ptychography) will be beneficial [28,29], though the extension to the 3D observation is not straightforward.

In x-ray diffraction microscopy using synchrotron radiation, the spatial resolution is often limited by the radiation damage [2] and/or by the statistical precision of the coherent diffraction data at high angles. The limitations will be removed or lowered dramatically with the x-ray free electron lasers (XFELs) currently being developed. The radiation damage can be reduced considerably by taking data before the sample is destroyed [21,30]. In such experiments, the stereo-3D imaging can be used to obtain 3D structural information [31]. Higher statistical precision can be obtained by focusing the XFEL beam to match the sample size [32,33]. We estimate from a simple flux calculation that a single focused XFEL pulse is enough for 2D reconstruction of a micrometer-sized sample by producing the coherent diffraction data at similar statistical accuracy to the present data, which currently takes about one hour to record.

Y. N. thanks A. Ito and K. Shinohara for the discussion on dose estimation. We thank K. Namba, J. Mizuki, T. Sutani and M. Nakasako for critical reading of the manuscript. This study was supported by KAKENHI, the Promotion of XFEL Research of MEXT, and a grant on Advanced Medical Technology from MHLW.

*nishino@spring8.or.jp

[1] *Cellular Electron Microscopy, Methods in Cell Biology*, edited by J. R. McIntosh (Academic Press, San Diego, 2007), Vol. 79.
[2] R. Henderson, Q. Rev. Biophys. **28**, 171 (1995).
[3] J. Kirz, C. Jacobsen, and M. Howells, Q. Rev. Biophys. **28**, 33 (1995).
[4] G. Schneider *et al.*, Surf. Rev. Lett. **9**, 177 (2002).
[5] W. Chao, B. D. Harteneck, J. A. Liddle, E. H. Anderson, and D. T. Attwood, Nature (London) **435**, 1210 (2005).
[6] A. Momose, Jpn. J. Appl. Phys. **44**, 6355 (2005).
[7] D. Sayre, Acta Crystallogr. **5**, 843 (1952).
[8] J. Miao, P. Charalambous, J. Kirz, and D. Sayre, Nature (London) **400**, 342 (1999).
[9] M. A. Pfeifer, G. J. Williams, I. A. Vartanyants, R. Harder, and I. K. Robinson, Nature (London) **442**, 63 (2006).
[10] J. R. Fienup, Appl. Opt. **21**, 2758 (1982).
[11] J. Miao, K. O. Hodgson, T. Ishikawa, C. A. Larabell, M. A. Le Gros, and Y. Nishino, Proc. Natl. Acad. Sci. U.S.A. **100**, 110 (2003).
[12] D. Shapiro *et al.*, Proc. Natl. Acad. Sci. U.S.A. **102**, 15 343 (2005).
[13] H. Jiang *et al.*, Phys. Rev. Lett. **100**, 038103 (2008).
[14] C. Song *et al.*, Phys. Rev. Lett. **101**, 158101 (2008).
[15] G. Schneider, Ultramicroscopy **75**, 85 (1998).
[16] J. R. Swedlow and T. Hirano, Mol. Cell **11**, 557 (2003).
[17] K. Maeshima and M. Eltsov, J. Biochem. (Tokyo) **143**, 145 (2008).
[18] K. Maeshima and U. K. Laemmli, Dev. Cell **4**, 467 (2003).
[19] Y. Nishino, J. Miao, and T. Ishikawa, Phys. Rev. B **68**, 220101 (2003).
[20] S. Marchesini *et al.*, Phys. Rev. B **68**, 140101(R) (2003).
[21] H. N. Chapman *et al.*, Nature Phys. **2**, 839 (2006).
[22] J. Miao, T. Ishikawa, B. Johnson, E. H. Anderson, B. Lai, and K. O. Hodgson, Phys. Rev. Lett. **89**, 088303 (2002).
[23] R. Mokso, P. Cloetens, E. Maire, W. Ludwig, and J. Y. Buffiere, Appl. Phys. Lett. **90**, 144104 (2007).
[24] G. C. Yin, F. R. Chen, Y. Hwu, H. P. D. Shieh, and K. S. Liang, Appl. Phys. Lett. **90**, 181118 (2007).
[25] S. Marchesini *et al.*, Opt. Express **11**, 2344 (2003).
[26] M. R. Howells *et al.*, arXiv:physics/0502059.
[27] R. Hegerl and W. Hoppe, Z. Naturforsch. **31A**, 1717 (1976).
[28] J. M. Rodenburg *et al.*, Phys. Rev. Lett. **98**, 034801 (2007).
[29] P. Thibault, M. Dierolf, A. Menzel, O. Bunk, C. David, and F. Pfeiffer, Science **321**, 379 (2008).
[30] R. Neutze *et al.*, Nature (London) **406**, 752 (2000).
[31] D. Sayre, Acta Crystallogr. Sect. A **64**, 33 (2008).
[32] G. J. Williams *et al.*, Phys. Rev. Lett. **97**, 025506 (2006).
[33] C. G. Schroer *et al.*, Phys. Rev. Lett. **101**, 090801 (2008).

Research Article

Spectrometry

Received: 30 June 2008 Revised: 7 October 2008 Accepted: 16 October 2008 Published online in Wiley Interscience: 26 November 2008

(www.interscience.com) DOI 10.1002/xrs.1123

Trace element mapping of a single cell using a hard x-ray nanobeam focused by a Kirkpatrick-Baez mirror system

S. Matsuyama,[a]* M. Shimura,[b] H. Mimura,[a] M. Fujii,[a] H. Yumoto,[c] Y. Sano,[a] M. Yabashi,[c] Y. Nishino,[d] K. Tamasaku,[d] T. Ishikawa[d] and K. Yamauchi[e,f]

To visualize the distributions of trace elements in biological samples such as tissues and cells at high spatial resolution, we developed a scanning x-ray fluorescence microscope (SXFM) at SPring-8, using a Kirkpatrick-Baez mirror optics that enables achromatic and highly efficient focusing. To evaluate performance regarding its application to biological samples, the SXFM was used at x-ray energy of 15 keV to observe NIH/3T3 cells in which adenosine triphosphate (ATP) synthase β (specifically localized at the mitochondria) were labeled with gold colloidal particles. Various elemental distributions were visualized at the single-cell level, including those for P, S, Cl, Ca, Fe, Cu, Zn and Au, and we obtained high-resolution elemental distribution maps by magnifying the labeled single mitochondrion. Maximum spatial resolution achieved in the experiments was sub-100 nm.

Introduction

X-ray fluorescence analysis has long been known as a powerful and accurate tool for obtaining elemental information. Recent rapid progress in hard x-ray focusing technology has enabled elemental mapping at sub-micron spatial resolutions.[1–3] In the field of cell biology, the importance of investigating elemental distributions has begun to be recognized, with several interesting studies having investigated intracellular elemental distributions.[4–10]

An elemental mapping using x-ray fluorescence analysis, which we call a scanning x-ray fluorescence microscope (SXFM), is one of the most suitable methods for visualizing elemental distributions in biological samples. The SXFM excitation beam consists of hard x-rays, which enables nondestructive observations of relatively thick samples under atmospheric conditions. In terms of spatial resolution, SXFMs employ short wavelengths, making them a more promising technique than visible light microscopes.[3] Compared with electron microscopes, SXFMs enable the ready acquisition of images of multielement distributions at sub-micron spatial resolution, without the requirement of complex sample-preparation techniques such as sectioning and coating of a conductive material.

We have studied x-ray mirrors as the focusing device for the hard x-rays.[11,12] X-ray mirrors are a promising device that potentially enable achromatic and highly efficient focusing.[13,14] We used our accumulated knowledge of hard x-ray focusing to develop a high-sensitivity, high-resolution SXFM system, using the powerful combination of a synchrotron radiation source, which can generate the brightest x-rays, and Kirkpatrick-Baez (K-B) mirrors[11,12,15] fabricated by our group.[16] In our previous work,[16] elemental distributions of fine test patterns could be visualized at a spatial resolution better than 50 nm. In this work, we visualized multielement distributions such as P, S, Cl, Ca, Fe, Cu, Zn and Au at the single-cell level in NIH/3T3 cells after clearly identifying the mitochondria by labeling adenosine triphosphate (ATP) synthase β (specifically localized at the mitochondria) with gold colloidal particles (5 nm in diameter) using an immunostaining method. By magnifying a single labeled mitochondrion, multiple elemental contents could be analyzed with sub-100 nm spatial resolution.

Materials and Methods

Scanning x-ray fluorescence microscope

Figure 1 shows the layout of our microscope. X-rays generated by a standard undulator at SPring-8 are monochromatized ($\Delta E/E = \sim 1.4 \times 10^{-4}$ at 15 keV) by a double-crystal [Si (111)] monochromator (DCM)[17] before being focused vertically and horizontally by a pair of elliptical mirrors (K-B mirrors) aligned at right angles to each other and placed approximately 100 m downstream of the undulator. The working distance is designed to be 100 mm in order to set up various components near samples

* Correspondence to: S. Matsuyama, Department of Precision Science and Technology, Graduate School of Engineering, Osaka University, 2-1 Yamada-oka, Suita, Osaka 565-0871, Japan. E-mail: matsuyama@prec.eng.osaka-u.ac.jp

a Department of Precision Science and Technology, Graduate School of Engineering, Osaka University, 2-1 Yamada-oka, Suita, Osaka 565-0871, Japan

b Department of Intractable Diseases, International Medical Center of Japan, 1-21-1 Toyama, Shinjuku-ku, Tokyo 162-8655, Japan

c SPring-8/Synchrotron Radiation Research Institute (JASRI), 1-1-1 Kouto, Sayoucho, Sayogun, Hyogo 679-5148, Japan

d SPring-8/RIKEN, 1-1-1 Kouto, Sayoucho, Sayogun, Hyogo 679-5148, Japan

e Department of Precision Science and Technology, Graduate School of Engineering, Osaka University, 2-1 Yamada-oka, Suita, Osaka 565-0871, Japan

f Research Center for Ultra-Precision Science and Technology, Graduate School of Engineering, Osaka University, 2-1 Yamada-oka, Suita, Osaka 565-0871, Japan

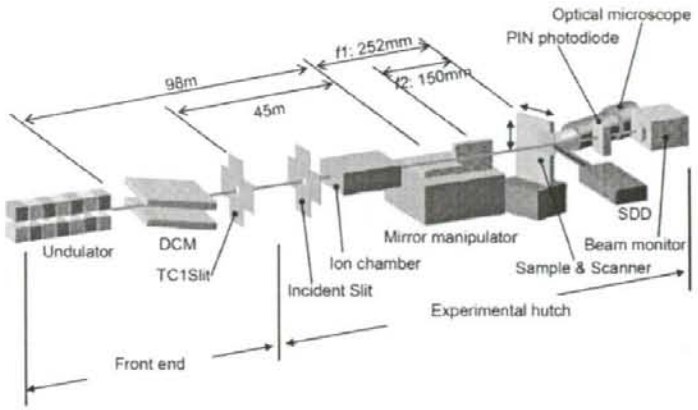

Figure 1. Layout of the SXFM system. Distance between the undulator and the first mirror is 98 m. The TC1Slit is placed 45 m upstream of the first mirror to form a virtual x-ray source. Focal lengths of the first and the second mirrors are 252 and 150 mm. The parameter of the elliptical mirrors is described in our previous study.[16]

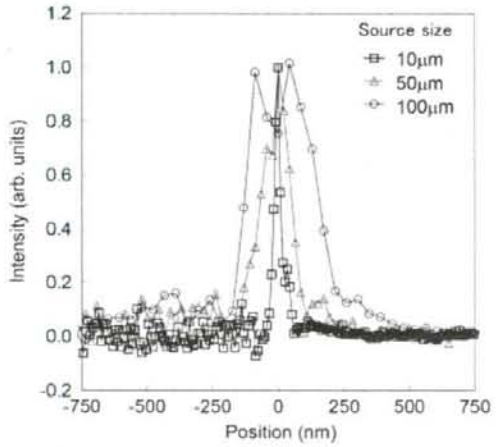

Figure 2. Profiles of typical x-ray beams used in the present study (direction: horizontal focusing, x-ray energy: 15 keV). The lines in the graph indicate the profiles measured by a wire scanning method with a gold wire of 0.2 mm diameter. The values shown in the graph indicated sizes of the virtual x-ray source formed by the TC1Slit. The narrowest beam has the full width at half maximum of 30 nm with the slit size of 10 μm.

in near future. The depth of focus is 50–200 μm depending on selected beam size, making it unnecessary to consider the thickness of thin samples such as cells. A noticeable point of our focusing system is that the beam size is controllable within a wide range, from 29 × 48 nm (diffraction limit) to ~2000 × ~2000 nm (at 15 keV), which is achieved by adjusting a slit (TC1Slit) installed just downstream of the DCM[16]; that is, we can select the optimum beam size for the scan area. Figure 2 shows profiles of the typical x-ray beam available in this microscope with the TC1Slit slit sizes of 10, 50 and 100 μm. The measured profiles in the graph show good controllability of beam size. An incident slit is placed just upstream of the x-ray mirrors to block unwanted x-rays and prevent them being received by the mirrors.

A mirror manipulator[18] developed specifically for the high-accuracy positioning of K-B mirrors enables rapid alignment of the mirrors with the accuracy required in diffraction-limited focusing. An energy dispersive detector (SDD, XFLASH DETECTOR Type 1201, Röntec Co., Ltd.) is employed to detect x-ray fluorescence with high sensitivity and high-energy resolution. A PIN photodiode is placed downstream from the sample stage to count transmission x-rays. An ion chamber is placed just upstream of the mirror manipulator to normalize output data that have intensity fluctuations. A linear-encoder-based feedback X-Y stage with a positioning resolution of 1 nm (SIGMA TECH Co., Ltd.) is used to obtain a high-resolution raster scan of the sample. The sample and the scanner are inclined at 60° to the incident x-ray beam to enable the SDD to be set up near the sample. The entire sample scanning system is hermetically enclosed in an acrylic box that is then filled with helium gas. Specifications of the SXFM system are summarized in

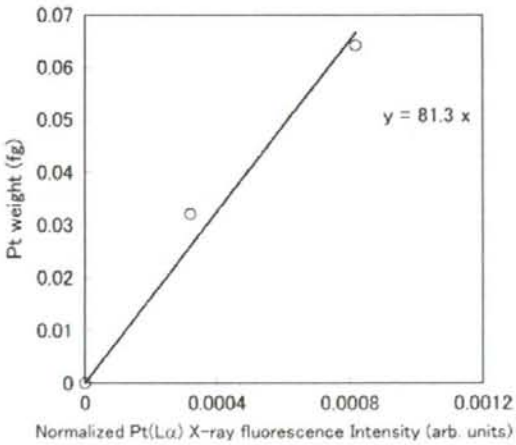

Figure 3. Linear calibration curve showing the relationship between weight of Pt and x-ray fluorescence Intensity (Pt Lα) normalized by the incident x-ray intensity.

Table 1. And the detail performance such as the best spatial resolution and beam stability was described in our previous study.[16]

Data analysis and semiquantitative analysis

X-ray fluorescence spectrum data detected by the SDD are sent to two multi-channel analyzers [(MCA), MCA8000A, AMPTEK Inc.] for pulse height analysis and are then downloaded to a personal computer (PC). One MCA transfers data to the PC while another processes data transferred from the SDD. X-ray fluorescence spectrum data (1024 channels) recorded for every pixel are processed using software developed to integrate the counts in each region of interest (ROI) selected in advance by the operator, as well as to visualize elemental distributions according to the ROIs. Recording a great deal of raw spectrum for every pixel in the PC enables background correction, noise reduction, and peak separation to be performed after the observations are completed. In the present study, a noise removal filter based on singular value decomposition[19] was used to improve the signal-to-noise ratio of the x-ray fluorescence spectrum, and then each fluorescence peak in the spectra is separated with a curve-fitting program, if necessary.

To quantitatively analyze the measured data, thin platinum membranes, of which the thickness and the density were measured in advance by Rutherford backscattering spectrometry (RBS), were measured under the same geometric conditions and the same beam condition as one of the sample observations. In the RBS system, ion species and beam size are helium nucleuses at an energy of 2.34 MeV and $1 \times 1\ mm^2$, respectively. On the basis of these results, a linear calibration curve of x-ray fluorescence intensity normalized by incident x-ray intensity was obtained as a function of the weight (fg) of platinum. In this case, the size of the focused beam and the exposure time were 30×50 nm

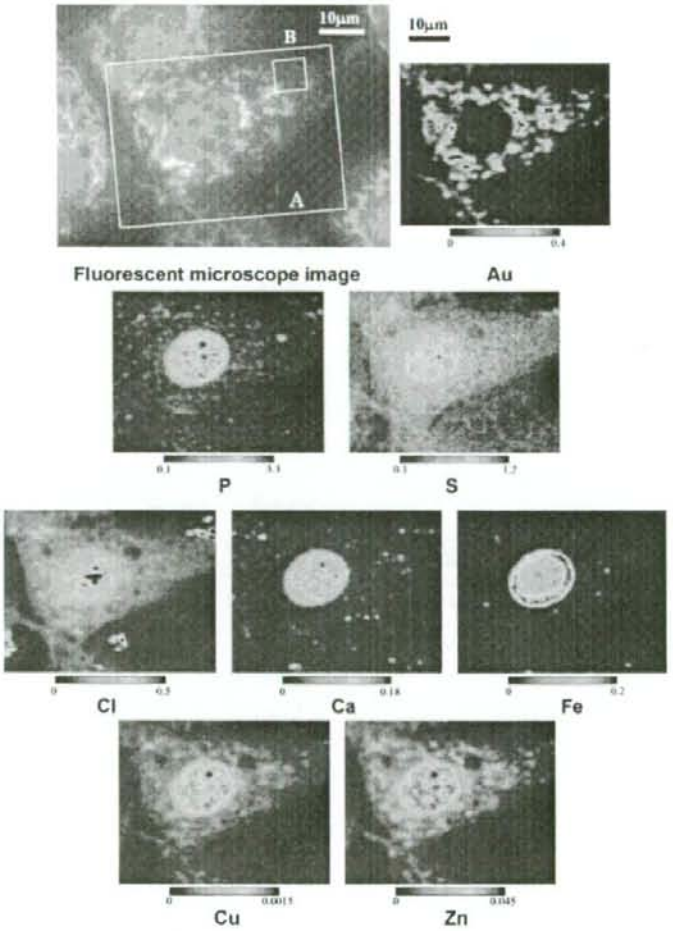

Figure 4. Fluorescent microscope image obtained using a visible light microscope and elemental distribution maps at a single-cell level in area A. The fluorescent microscope image and the Au distribution map show the existence of ATP synthase β, localized in mitochondria. Color bars indicate the elemental contents (fg) in an irradiation area.

Table 1. System specifications for the SXFM

	Vertical direction	Horizontal direction
Mirror aperture	382 μm	365 μm
Numerical aperture	0.75×10^{-3}	1.20×10^{-3}
Working distance	100 mm	
Depth of focus[a]	>150 μm	>50 μm
Available x-ray energy	4.4 ~ 19 keV at BL29XUL of SPring-8	
Available beam size (H × V)	29×48~2000×2000 nm^2	
Available photon flux	6×10^8~8×10^{11} photons/s	
Minimum step size	1 nm	
Maximum scan range	20×20 mm^2	

[a] Depth of focus is defined as the tolerance of focal length where the focus-size broadening is within 10%. It depends on source size; the depth of focus values given in the table were calculated under a diffraction-limited condition.

and 1 s, respectively. The linear calibration curve shown in Fig. 3 was obtained from this analysis. The contents of other elements were determined semiquantitatively using the calibration curve and ratio of x-ray emission efficiency. The efficiency was estimated by the equation:

$$\beta_i = \mu_i \cdot \omega_i \cdot K_i \cdot R_i^p$$

where β_i is the coefficient of x-ray emission efficiency depending on individual elements of i. The parameters μ_i and ω_i represent the photoelectric mass absorption and fluorescence yield, respectively, of element i. The parameters K_i and R_i^p are, respectively, the absorption jump ratio of the corresponding atomic shell in element i and the intensity fraction of the p-line to the entire emission series to which the p-line belongs in the element i. Linear calibration curves of respective elements were estimated with β_i, β_{Pt} and the calibration curve of Pt.

$$\gamma_i = \varepsilon_i \cdot \gamma_{Pt} \cdot \beta_{Pt}/\beta_i$$

where γ_i and ε_i are the slope of the linear calibration curve of the element i, and the detector efficiency. Details of semiquantitative determination are described in our previous work.[20] Detection of light elements such as P, S, Cl and Ca are affected by self-absorption effects. In the experiments, the effects are not corrected for, so that the semiquantitative determination of light elements may lead to errors. At a rough estimate from thickness of a cell (5 μm) and a support film (prolen, 4 μm), signal losses of ~10% (3 keV), ~30% (2 keV) and ~90% (1 keV) occur. Additionally, after we confirmed the uncertainty of the semiquantitative determination in other experiments, it was found to be ±9.5% (standard deviations) in Si, Ni and Pt.

Table 2. Scan parameters for observations of the cells

	Area A	Area B
Scan method	Raster scan	Raster scan
X-ray energy (keV)	15	15
Beam size (nm, H × V)	500 × 500	70 × 70
Scanning pitch (nm)	500	70
Scan area (μm, H × V)	50 × 38	7 × 7
Exposure time (s/pixel)	1	2

Cell culture and preparation

NIH/3T3 cells, plated on a prolene film (4-μm thickness, Chemplex Industries, Inc.) sterilized by 70% ethanol, were cultured in Dulbecco's modified Eagle's medium (Sigma-Aldrich) supplemented with 10% fetal bovine serum (Sigma-Aldrich) for 48 h at 37 °C, 5% CO_2. Cells were washed by phosphate buffer saline (PBS) and fixed with 4% paraformaldehyde in PBS for 10 min. Cells were permeabilized with PBS containing 0.2% Triton X-100 (Sigma-Aldrich) for 5 min. As much as 10% goat serum in PBS containing 0.05% Tween 20 (PBST) was used for blocking. ATP synthase β (1 : 200, MA1-930, Affinity BioReagents, Inc.) was applied with a primary antibody. After washing three times by PBST, cells were incubated with biotinylabeled anti-mouse IgG (B6649) (1 : 100, Sigma-Aldrich) for 30 min at 37 °C. Cells were then incubated with a mixture of gold-conjugated (58-30-06)(1 : 10, Kirkegaard & Perry Laboratories, Inc.) and FITC-conjugated (E2761)(1 : 50, Sigma-Aldrich) avidins for 30 min at room temperature. Fluorescence images were taken by CCD camera (DS-5Mc, Nikon Corporation) and software (ACT-2U, Nikon Corporation) (Fig. 4) prior to rinsing the film with 80% ethanol. The film was dried at room temperature for the SXFM.

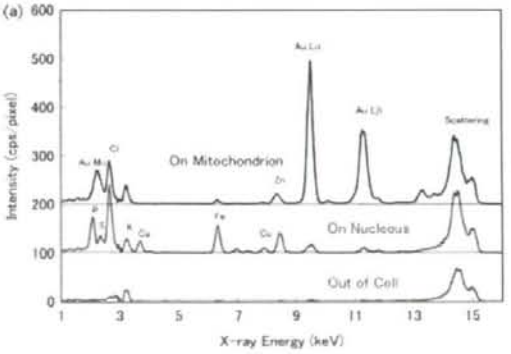

Typical spectra in Fig. 4

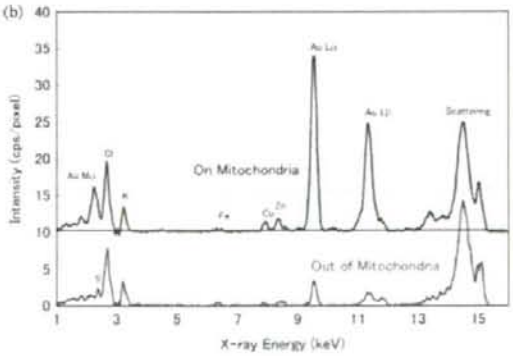

Typical spectra in Fig. 6

Figure 5. Typical x-ray fluorescence spectra recorded for each pixel in the elemental maps shown in Figs 4 and 6. Peaks of Ar are removed with a peak fitting program to reveal the peaks near 3 keV. Although the samples and the detector were in a helium atmosphere, an accident in helium purge caused unintended argon contamination.

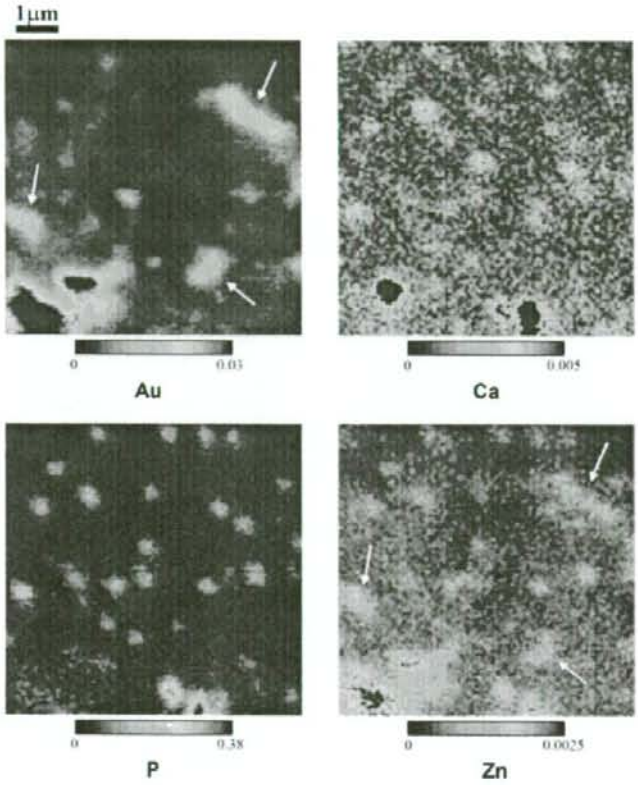

Figure 6. High-resolution elemental distribution maps in area B in Fig. 4. The elliptical object indicated by arrows in the Au distribution map shows a single mitochondrion and the dense region at the lower left represents the piles of mitochondria. Color bars indicate the elemental contents (fg) in an irradiation area.

Results and Discussion

Cells were observed at the second experimental hutch (EH2) of BL29XUL[21] at SPring-8. X-ray energy of 15 keV was selected to enable the detection of elements from Na (Z = 11) to Pb (Z = 82) using x-ray fluorescence. In this experiment, the temperature of the whole SXFM system was maintained within ±0.1 °C to ensure the stability of beam position and size. Elemental distribution maps obtained by SXFM at the single-cell level are shown in Fig. 4. Table 2 shows the scanning parameters used. Typical spectra recorded for each pixel are shown in Fig. 5. The color bars shown in Fig. 4 indicate the elemental contents (fg), which are semiquantitatively determined as mentioned above, within an irradiation area. As can be seen from the elemental distribution maps, the Au distribution image obtained by SXFM was consistent with the fluorescence image obtained using a visible light microscope. We confirmed in pilot studies that mitochondrial fluorescence signals obtained in the above manner colocalized with the signal obtained by Mitored (Dojindo Molecular Technologies, Inc.), which localizes at mitochondria and emits red fluorescence (data not shown). Therefore, Au distribution corresponds to mitochondria localization at the light microscope level. Compared with other elements, Zn and Cu are particularly colocalized with Au distribution, except for the nucleus, while P, Ca and Fe are highly concentrated at the nucleus. Similar distributions were obtained in all seven cells observed by our SXFM.

To acquire higher-resolution images of the mitochondria, the beam was sharpened by closing the TC1Slit. Figure 6 shows high-resolution elemental distribution maps. Although Cu distribution maps could not be obtained due to the poor signal-to-noise ratio of the images, other elemental distributions could be visualized at a high resolution (maps of S, Cl and Fe not shown). As can be seen from the distribution maps, the signal intensities of Zn were partially colocalized with Au (indicated by arrow). The signal intensities of Ca, P and Zn, which appear granular, are likely to correspond to other organelles that could not be identified in the experiments. If the distribution of a particular element corresponds to the distribution of an organelle, we may be able to utilize elemental distributions as organelle markers. On the basis of the obtained Zn map, Zn is likely to have potential as a mitochondrial marker.

Conclusions

A scanning x-ray fluorescence microscope developed by installing a K-B mirror system at SPring-8 enabled observations of trace element distributions in biological samples at high spatial

resolution. Observation of cells resulted in visualization of various elemental distributions, including P, S, Cl, Ca, Fe, Cu, Zn and Au. In terms of spatial resolution, resolution better than 100 nm was obtained in the magnified elemental maps. The focusing system developed in the present study enables the formation of a nanobeam with full width at half maximum of 30 nm[16]; this will enable the detection of intracellular elemental distributions with a resolution of 30 nm in the near future.

Acknowledgements

This research was supported by a Grant-in-Aid for Specially Promoted Research 18002009, 2006 and 21st Century COE Research, Center for Atomistic Fabrication Technology, 2006, from the Ministry of Education, Sports, Culture, Science and Technology, Japan, and a Research on Advanced Medical Technology 2006-11-29, 2006, from Ministry of Health, Labor and Welfare, Japan. We thank Ms. Keiko Katagishi for help with cell cultures and sample preparation.

References

[1] C. H. Kang, J. Maser, B. G. Stephenson, C. Liu, R. Conley, T. A. Macrander, S. Vogt, *Phys. Rev. Lett.* **2006**, *96*, 127401.
[2] Y. Suzuki, A. Takeuchi, H. Takano, H. Takenaka, *Jpn. J. Appl. Phys.* **2005**, *44*, 4A 1994.
[3] H. Mimura, H. Yumoto, S. Matsuyama, Y. Sano, K. Yamamura, Y. Mori, M. Yabashi, Y. Nishino, K. Tamasaku, T. Ishikawa, K. Yamauchi, *Appl. Phys. Lett.* **2007**, *90*, 051903.
[4] C. Meinecke, M. Morawski, T. Reinert, T. Arendt, T. Butz, *Nucl. Instrum. Methods Phys. Res.* **2006**, *B249*, 688.
[5] H. Sakurai, M. Okamoto, M. Hasegawa, T. Satoh, M. Oikawa, T. Kamiya, K. Arakawa, T. Nakano, *Cancer Sci.* **2008**, *99*, 901.
[6] M. Morello, A. Canini, P. Mattioli, P. R. Sorge, A. Alimonti, B. Bocca, G. Forte, A. Martorana, G. Bernardi, G. Sancesario, *Neurotoxicology* **2008**, *29*, 60.
[7] V. M. Zoriy, M. Dehnhardt, A. Matusch, S. J. Becker, *Spectrochim. Acta, Part B* **2008**, *63*, 375.
[8] M. Dickinson, P. J. Heard, J. H. A. Barker, A. C. Lewis, D. Mallard, G. C. Allen, *Appl. Surf. Sci.* **2006**, *252*, 6793.
[9] R. McRae, B. Lai, S. Vogt, J. C. Fahrni, *J. Struct. Biol.* **2006**, *155*, 22.
[10] M. Shimura, A. Saito, S. Matsuyama, T. Sakuma, Y. Terui, K. Ueno, H. Yumoto, K. Yamauchi, K. Yamamura, H. Mimura, Y. Sano, M. Yabashi, K. Tamasaku, K. Nishio, Y. Nishino, K. Endo, K. Hatake, Y. Mori, Y. Ishizaka, T. Ishikawa, *Cancer Res.* **2005**, *65*, 4998.
[11] K. Yamauchi, K. Yamamura, H. Mimura, Y. Sano, A. Saito, K. Endo, A. Souvorov, M. Yabashi, K. Tamasaku, T. Ishikawa, Y. Mori, *Jpn. J. Appl. Phys.* **2003**, *42*, 7129.
[12] H. Mimura, S. Matsuyama, H. Yumoto, H. Hara, K. Yamamura, Y. Sano, M. Shibahara, K. Endo, Y. Mori, Y. Nishino, K. Tamasaku, M. Yabashi, T. Ishikawa, K. Yamauchi, *Jpn. J. Appl. Phys.* **2005**, *44*, 539.
[13] W. Liu, E. G. Ice, Z. J. Tischler, A. Khounsary, C. Liu, L. Assoufid, T. A. Macrander, *Rev. Sci. Instrum.* **2005**, *76*, 113701.
[14] O. Hignette, P. Cloetens, G. Rostaing, P. Bernard, C. Morawe, *Rev. Sci. Instrum.* **2005**, *76*, 063709.
[15] P. Kirkpatrick, A. V. Baez, *J. Opt. Soc. Am.* **1948**, *38*, 766.
[16] S. Matsuyama, H. Mimura, H. Yumoto, Y. Sano, K. Yamamura, M. Yabashi, Y. Nishino, K. Tamasaku, T. Ishikawa, K. Yamauchi, *Rev. Sci. Instrum.* **2006**, *77*, 103102.
[17] T. Mochizuki, Y. Kohmura, A. Awaji, Y. Suzuki, A. Baron, K. Tamasaku, M. Yabashi, H. Yamazaki, T. Ishikawa, *Nucl. Instrum. Methods* **2001**, *A467/468*, 647.
[18] S. Matsuyama, H. Mimura Yumoto, H. Hara, K. Yamamura, Y. Sano, K. Endo, Y. Mori, M. Yabashi, Y. Nishino, K. Tamasaku, T. Ishikawa, K. Yamauchi, *Rev. Sci. Instrum.* **2006**, *77*, 093107.
[19] N. Uzunbajakava, A. Lenferink, Y. Kraan, E. Volokhina, G. Vrensen, J. Greve, C. Otto, *Biophys. J.* **2003**, *84*, 3968.
[20] S. Matsuyama, H. Mimura, K. Katagishi, H. Yumoto, S. Handa, M. Fujii, Y. Sano, M. Shimura, M. Yabashi, Y. Nishino, K. Tamasaku, T. Ishikawa, K. Yamauchi, *Surf. Interface Anal.* **2008**, *40*, 1042.
[21] K. Tamasaku, Y. Tanaka, M. Yabashi, H. Yamazaki, N. Kawamura, M. Suzuki, T. Ishikawa, *Nucl. Instrum. Methods* **2001**, *467*, 686.

Research Article

Received: 19 October 2007 Revised: 22 January 2008 Accepted: 22 January 2008 Published online in Wiley Interscience: 7 March 2008

(www.interscience.com) DOI 10.1002/sia.2844

Trace element mapping using a high-resolution scanning X-ray fluorescence microscope equipped with a Kirkpatrick-Baez mirror system

S. Matsuyama,[a]* H. Mimura,[a] K. Katagishi,[a] H. Yumoto,[a] S. Handa,[a] M. Fujii,[a] Y. Sano,[a] M. Shimura,[b] M. Yabashi,[c] Y. Nishino,[d] K. Tamasaku,[d] T. Ishikawa[d] and K. Yamauchi[a,e]

We have developed a scanning X-ray fluorescence microscope (SXFM) using Kirkpatrick-Baez mirror optics, which enables achromatic and highly efficient focusing, at BL29XUL of SPring-8. The SXFM enables observations of multielement distributions inside a sample with high resolution and high sensitivity. Previously, we have reported the high spatial resolution of a newly developed SXFM. In the present paper, we focus on the high sensitivity of the SXFM. By observations of fine test patterns using the X-ray beam probe having a size of 100 × 100 nm² and an energy of 15 keV, the lower detection limit for the visualization of elemental distributions was investigated. As a result, the lower detection limits were found to be 0.009 fg (gallium) and 0.012 fg (tungsten).

Keywords: scanning X-ray fluorescence microscope; X-ray microscopy; Kirkpatrick-Baez mirror system; trace element mapping; hard X-ray; focusing

Introduction

The measurement of elemental distributions has been widely applied to impurity analysis inside semiconductors and metals in materials science. Recently, the importance of such a measurement technique has begun to be recognized in various fields, such as biology, medical science, and archaeology, and several interesting studies using new methods to measure elemental distributions have been reported.[1–4] However, few observational techniques have high resolution, high sensitivity, and simultaneous multielement detection capabilities that can be used under atmospheric conditions.

A scanning X-ray fluorescence microscope (SXFM) is a spectromicroscope that allows quantitative elemental maps to be acquired using X-ray fluorescence analysis, a focused hard X-ray beam, and raster scanning of a specimen. Since the excitation beam consists of hard X-rays, an SXFM enables us to observe samples without causing destruction and under atmospheric conditions. From the viewpoint of spatial resolution, SXFMs are more promising than visible light microscopes owing to the short wavelengths. Compared to other microscopes, SXFMs allow for easy acquisition of images of multielement distributions at a sub-100-nm spatial resolution without complex sample preparation under atmospheric conditions.

We have developed a high-sensitivity, high-resolution SXFM using the powerful combination of a synchrotron radiation source, which can generate the brightest X-rays, and a Kirkpatrick-Baez (K-B) mirror system,[5–7] which enables achromatic and highly efficient focusing. Previously, we reported the high spatial resolution of the SXFM.[8] In the present paper, the high sensitivity of the SXFM is considered. In order to investigate lower detection limits for the purpose of visualizing elemental distributions, fine test patterns were observed. Moreover, the data of X-ray fluorescence obtained by the SXFM were quantified using standard specimens, the elemental contents of which were determined by Rutherford backscattering spectrometry (RBS). As a result, the detection limits were found to be 0.009 fg (gallium) and 0.012 fg (tungsten). In this experiment, the hard X-ray probe had a size of 100 × 100 nm² and an energy of 15 keV.

* *Correspondence to: S. Matsuyama, Department of Precision Science and Technology, Graduate School of Engineering, Osaka University, 2-1 Yamada-oka, Suita, Osaka 565-0871, Japan.*
E-mail: matsuyama@prec.eng.osaka-u.ac.jp

a *Department of Precision Science and Technology, Graduate School of Engineering, Osaka University, 2-1 Yamada-oka, Suita, Osaka 565-0871, Japan*

b *Department of Intractable Diseases, International Medical Center of Japan, 1-21-1 Toyama, Shinjuku-ku, Tokyo 162-8655, Japan*

c *SPring-8/Synchrotron Radiation Research Institute (JASRI), 1-1-1 Kouto, Sayoucho, Sayogun, Hyogo 679-5148, Japan*

d *SPring-8/RIKEN, 1-1-1 Kouto, Sayoucho, Sayogun, Hyogo 679-5148, Japan*

e *Research Center for Ultra-Precision Science and Technology, Graduate School of Engineering, Osaka University, 2-1 Yamada-oka, Suita, Osaka 565-0871, Japan*

Experimental

Scanning X-ray fluorescence microscope

Figure 1 shows the optical focusing system employed in the proposed X-ray microscope. X-rays generated by an undulator are monochromatized to approximately 0.014% (at 15 keV) by a double-crystal monochromator (DCM)[9] and then focused by a pair of elliptical mirrors aligned at a right angle to each other for vertical and horizontal focusing, called a Kirkpatrick-Baez (K-B) mirror system,[8] and placed approximately 100 m downstream of the undulator. The working distance is designed to be 100 mm considering the practical use of the X-ray microscope. One major feature of the focusing system is that the beam size is controllable within a wide range from 29 × 48 nm^2 (theoretical diffraction limit) to ~2000 × ~2000 nm^2 (at 15 keV) by adjusting a slit installed just downstream of the DCM.[8]

Figure 2 shows a schematic diagram of the SXFM system. A mirror manipulator,[10] developed especially for high-accuracy positioning of K-B mirrors, allows for the rapid alignment of two mirrors with an accuracy required for diffraction-limited focusing. A PIN photodiode is placed downstream of the sample stage to count transmission X-rays. An ion chamber is placed just upstream of the mirror manipulator to normalize output data having intensity fluctuations. An energy dispersive detector (silicon drift detector, SDD, Röntec Co., Ltd.) is employed to detect X-ray fluorescence with high sensitivity and high-energy resolution. A sample and a linear-encoder-based feedback X–Y stage with a positioning resolution of 1 nm (SIGMA TECH, Co., Ltd.) are inclined at 60° to the incident X-ray beam to set up the SDD near the sample. The entire sample scanning system can be hermetically enclosed using an acrylic box and filled with helium gas.

X-ray fluorescence data detected by the SDD are analyzed by a multichannel analyzer (MCA, MCA8000A, AMPTEK Inc.) for pulse height analysis and are then downloaded to a personal computer. X-ray fluorescence spectrum data recorded for every pixel are processed using newly developed software, which integrates the counts of each region of interest (ROI) selected by the user in advance and visualizes elemental distributions according to the ROIs.

Quantitative analysis

To quantitatively analyze the measured data, thin membranes coated with platinum and nickel, the thickness and density of which were determined in advance by RBS, were measured under the same geometric conditions and the same beam condition as one of sample observations. In the RBS system, ion species are helium nucleuses at an energy of 2.34 MeV and a beam size of 1 × 1 mm^2. On the basis of on these results, a linear calibration curve of normalized X-ray fluorescence intensity as a function of the weight (fg) of platinum and nickel, having thicknesses of approximately 1 and 2 nm, was obtained (Fig. 3). In this case, the size of the focused beam and the exposure time were 100 × 100 nm^2 and 1 s, respectively, and the number of measurements is 100. When

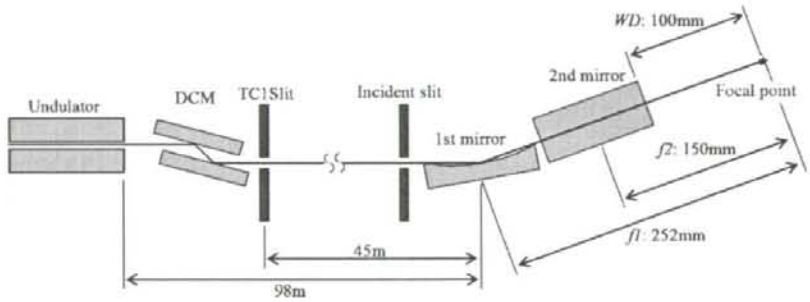

Figure 1. Optical focusing system.

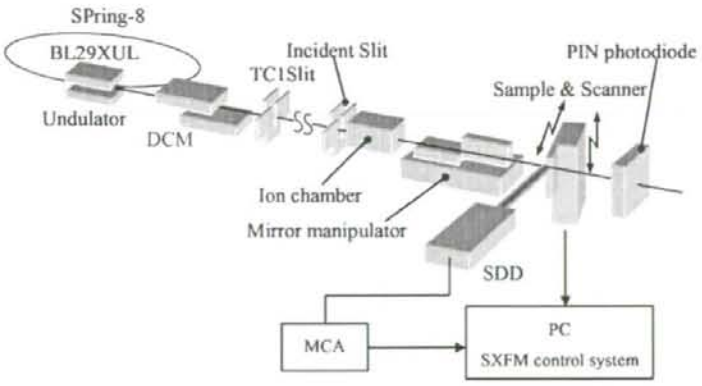

Figure 2. Scanning X-ray fluorescence microscope system.

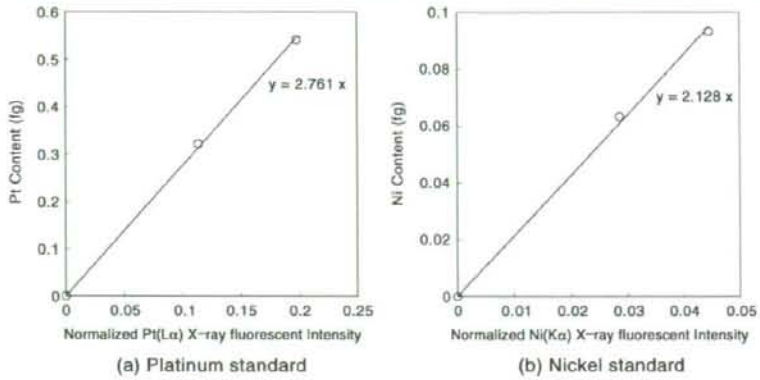

Figure 3. Linear calibration curves of normalized X-ray fluorescence intensity as a function of weight (fg). The weight on the vertical axis is decided by Rutherford backscattering spectrometry. Thick standard: $9.57 \pm 0.37 \times 10^{15}$ (atoms/cm^2: Ni), $1.67 \pm 0.05 \times 10^{16}$ (atoms/cm^2: Pt). Thin standard: $6.50 \pm 0.28 \times 10^{15}$ (atoms/cm^2: Ni), $9.92 \pm 0.28 \times 10^{15}$ (atoms/cm^2: Pt).

self-absorption effects and matrix effects are negligibly small because of a thin and/or sparse specimen and the incident X-ray is monochromatic, the contents of other elements were semi-quantitatively determined using the achieved calibration curve and the simple equations[11] below:

$$I(ip) = I_0 \cdot (\mu_i \cdot W_i \cdot \omega_i \cdot K_i \cdot R_i^p) \cdot T(ip) \cdot \varepsilon(ip) \cdot G \quad (1)$$

$$\beta_i = (\mu_i \cdot \omega_i \cdot K_i \cdot R_i^p) \cdot T(ip) \cdot \varepsilon(ip) \quad (2)$$

$$1/\alpha_i = \beta_i \cdot G = 1/\alpha_{pt} \cdot \beta_i/\beta_{Pt} = 1/\alpha_{Ni} \cdot \beta_i/\beta_{Ni} \quad (3)$$

$$W_i = \alpha_i \cdot (I(ip)/I_0) \quad (4)$$

where α_i and β_i are coefficients depending on individual elements of i. Specifically, α_i denotes the slope of the linear calibration curve. In addition, $I(ip)$ and I_0 are the X-ray fluorescence intensities of the p-line in the element i, corresponding to counts accumulated into the ROI and the incident X-ray intensity given by the ion chamber, respectively, and W_i is the weight of element i in the irradiated area. The parameters μ_i and ω_i represent the photoelectric mass absorption and fluorescence yield, respectively, of element i. Parameters K_i and R_i^p are, respectively, the absorption jump ratio of the corresponding atomic shell in element i and the intensity fraction of the p-line to the entire emission series to which the p-line belongs in the element i. The parameters G, $T(ip)$, and $\varepsilon(ip)$, which correct the efficiency of X-ray fluorescence emission, indicate a geometrical factor, the transmission through the atmosphere between the sample and the SDD, and the detector efficiency of the SDD, respectively. The $\varepsilon(ip)$ corresponds to the value measured by the manufacturer. The other parameters except ε in these equations were obtained through the X-ray data booklet.[12]

Results and Discussion

To investigate the lower detection limit of the SXFM, observations of the test patterns were performed at the second experimental hutch (EH2) of BL29XUL of SPring-8 at an X-ray energy of 15 keV. The patterns used in the present study were microfabricated on a thin SiN membrane (NTT Advanced Technology Corporation Co., Ltd.) using a focused ion beam system (Hitachi, Co., Ltd., FB-2100). Figure 4(a) shows the fabricated pattern, in which the white area represents a tungsten deposition. Elemental distribution maps visualized by the SXFM are shown in Figs 4(b) and (c). The color bars shown in Fig. 4 indicate the content (fg) of the element existing in the irradiation area (100×100 nm^2). The two maximum and minimum values represent values quantified using the two standard specimens of nickel (upper) and platinum (lower), respectively. In the case of Fig. 4, data mismatching falls within 20%. This result suggests that the proposed quantitative analysis is properly processed.

We estimated the detection limits for visualizing elemental distributions in the case of Fig. 4 using the following equation:

$$MDL = 3\sqrt{B}/I_0 \cdot \alpha \quad (5)$$

where MDL denotes the method detection limit (fg), I_0 is the incident X-ray intensity (count), $\sqrt{B}$, in which B is the background level (count) in each raw X-ray fluorescence intensity map before quantitative analysis, denotes the standard deviation of shot noise (count), and the parameter α is the slope of the linear calibration curve mentioned in Eqn (4). As a result of the calculation, MDLs to visualize elemental distributions were found to be 8.8×10^{-3} (fg, gallium) and 12×10^{-3} (fg, tungsten) under the condition of a dwell time of 1 s and a beam size of 100×100 nm^2 (Table 1). In the analysis, the background level is estimated to be 3 (tungsten) ~6 (gallium, silicon) cps per channel of the SDD using the histogram of the elemental maps. However, the value actually includes not only background noise but also signals, considering X-ray fluorescence spectra recorded for each pixel. Therefore, the real background levels of these are thought to be approximately 1 cps per channel. Real MDLs appear to be smaller than the values calculated above.

Table 1. Estimated lower detection limits

	B (count)	α/I_0 (fg/count)	MDL (fg)
Si	230	24.5×10^{-3}	1.11
Ga	220	0.197×10^{-3}	8.76×10^{-3}
W	119	0.361×10^{-3}	11.8×10^{-3}

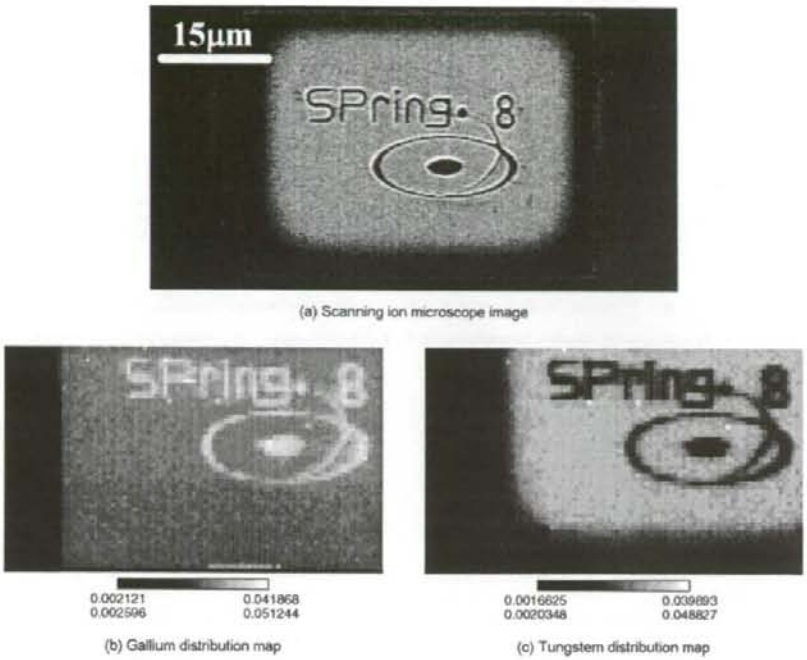

Figure 4. Scanning ion microscope image (a) and elemental distributions (b)(c) of the test pattern. The two maximum and minimum values in (b)(c) represent values quantified using the standard specimens of nickel (upper) and platinum (lower), respectively. (X-ray energy: 15 keV, Beam size: 100 nm × 100 nm, Scanning pitch: 100 nm/pixel, dwell time: 1 s/pixel).

Conclusions

These experiments and analyses show that the developed SXFM can visualize elemental distributions in which the contents of gallium and tungsten are on the order of 0.01 fg using a nanobeam having a size of 100 × 100 nm^2. This high sensitivity enables us to investigate samples of minute size and samples that contain trace elements, such as cells and tissues. To improve the sensitivity of the proposed SXFM, the development of long focusing mirrors and an X-ray detector having a large active area is necessary, and the former improvement is currently being investigated by our group. In the near future, using the SXFM, we hope to obtain new insights into various scientific fields based on element distributions.

Acknowledgements

This research was supported by a Grant-in-Aid for Specially Promoted Research 18002009, 2006 and 21st Century COE Research, Center for Atomistic Fabrication Technology, 2006, from the Ministry of Education, Sports, Culture, Science and Technology, Japan, and a Research on Advanced Medical Technology 2006-11-29, 2006, from Ministry of Health, Labor and Welfare, Japan.

References

[1] Kemner KM, Kelly SD, Lai B, Maser J, O'Loughlin EJ, Sholto-Douglas D, Cai Z, Schneegurt MA, Kulpa CF Jr, Nealson KH. *Science.* 2004; **22**: 686.
[2] Shimura M, Saito A, Matsuyama S, Sakuma T, Terui Y, Ueno K, Yumoto H, Yamauchi K, Yamamura K, Mimura H, Sano Y, Yabashi M, Tamasaku K, Nishio K, Nishino Y, Endo K, Hatake K, Mori Y, Ishizaka Y, Ishikawa T. *Cancer Res.* 2005; **65**: 4998.
[3] Strick R, Strissel PL, Gavrilov K, Levi-Setti R. *J. Cell Biol.* 2001; **155**: 899.
[4] Zoriy MV, Dehnhardt M, Reifenberger G, Zilles K, Becker JS. *Int. J. Mass spectrom.* 2006; **257**: 27.
[5] Kirkpatrick P, Baez AV. *J. Opt. Soc. Am.* 1948; **38**: 766.
[6] Yamauchi K, Yamamura K, Mimura H, Sano Y, Saito A, Endo K, Souvorov A, Yabashi M, Tamasaku K, Ishikawa T, Mori Y. *Jpn. J. Appl. Phys.* 2003; **42**: 7129.
[7] Mimura H, Matsuyama S, Yumoto H, Hara H, Yamamura K, Sano Y, Shibahara M, Endo K, Mori Y, Nishino Y, Tamasaku K, Yabashi M, Ishikawa T, Yamauchi K. *Jpn. J. Appl. Phys.* 2005; **44**: 539.
[8] Matsuyama S, Mimura H, Yumoto H, Sano Y, Yamamura K, Yabashi M, Nishino Y, Tamasaku K, Ishikawa T, Yamauchi K. *Rev. Sci. Instrum.* 2006; **77**: 103102.
[9] Mochizuki T, Kohmura Y, Awaji A, Suzuki Y, Baron A, Tamasaku K, Yabashi M, Yamazaki H, Ishikawa T. *Nucl. Instrum. Methods* 2001; **A467/468**: 647.
[10] Matsuyama S, Mimura H, Yumoto H, Hara H, Yamamura K, Sano Y, Endo K, Mori Y, Yabashi M, Nishino Y, Tamasaku K, Ishikawa T, Yamauchi K. *Rev. Sci. Instrum.* 2006; **77**: 093107.
[11] Shiraiwa T, Fujino N. *Jpn. J. Appl. Phys.* 1966; **5**: 886.
[12] Thompson AC, Attwood DT, Gullikson EM, Howells MR, Kortright JB, Robinson AL, Underwood JH, Kim K, Kirz J, Lindau I, Pianetta P, Winick H, Williams GP, Scofield JH. In *X-Ray Data Booklet*, Thompson AC, Vaughan D (eds). Lawrence Berkeley National Laboratory: California, 2001.

Analysis of cryo-electron microscopy images does not support the existence of 30-nm chromatin fibers in mitotic chromosomes in situ

Mikhail Eltsov[a,b,1,2], Kirsty M. MacLellan[a,c,1], Kazuhiro Maeshima[d,1], Achilleas S. Frangakis[b,e], and Jacques Dubochet[a,f]

[a]Laboratoire d'Analyse Ultrastructurale, Université de Lausanne, Biophore, CH-1015, Lausanne, Switzerland; [d]Cellular Dynamics Laboratory, RIKEN, 2-1, Hirosawa, Wako-shi, Saitama, 351-0198, Japan; [b]European Molecular Biology Laboratory, Meyerhofstrasse 1, D-69117 Heidelberg, Germany; [c]Institut de Minéralogie et de Physique des Milieux Condensés, Université Pierre et Marie Curie, IMPMC-UMR7590, Paris F-75005, France; and [f]Département d'Ecologie et d'Evolution, Université de Lausanne, Biophore, CH-1015, Lausanne, Switzerland; and [e]Cluster of Excellence Macromolecular Complexes, Johann Wolfgang Goethe University, Max-von-Laue-Strasse 1, Frankfurt D-60438, Germany

Communicated by Nancy Kleckner, Harvard University, Cambridge, MA, October 10, 2008 (received for review August 5, 2008)

Although the formation of 30-nm chromatin fibers is thought to be the most basic event of chromatin compaction, it remains controversial because high-resolution imaging of chromatin in living eukaryotic cells had not been possible until now. Cryo-electron microscopy of vitreous sections is a relatively new technique, which enables direct high-resolution observation of the cell structures in a close-to-native state. We used cryo-electron microscopy and image processing to further investigate the presence of 30-nm chromatin fibers in human mitotic chromosomes. HeLa S3 cells were vitrified by high-pressure freezing, thin-sectioned, and then imaged under the cryo-electron microscope without any further chemical treatment or staining. For an unambiguous interpretation of the images, the effects of the contrast transfer function were computationally corrected. The mitotic chromosomes of the HeLa S3 cells appeared as compact structures with a homogeneous grainy texture, in which there were no visible 30-nm fibers. Power spectra of the chromosome images also gave no indication of 30-nm chromatin folding. These results, together with our observations of the effects of chromosome swelling, strongly suggest that, within the bulk of compact metaphase chromosomes, the nucleosomal fiber does not undergo 30-nm folding, but exists in a highly disordered and interdigitated state, which is, on the local scale, comparable with a polymer melt.

chromatin compaction | polymer melt | chromosome structure | vitreous sections | contrast | transfer function

The degree of mitotic DNA compaction, which is essential for successful segregation of chromatids between daughter cells, is remarkable in that the mitotic chromatid in humans is >10,000 times shorter than the original DNA molecule (1). The most basic DNA compaction in eukaryotes occurs through the wrapping of DNA around octamers of core histone proteins (H2A, H2B, H3, and H4) (2, 3). This step results in a repetitive motif that is composed of nucleosomes alternated with naked "linker DNA," which is classified as the basic chromatin unit or the first level of DNA compaction (4). The subsequent folding of the basic chromatin fiber into the 0.7-μm thick chromatid seen at metaphase remains unclear, although it is known that condensins and topoisomerase IIα are implicated in this process (for recent reviews, see refs. 5–7). These proteins are variously assumed to mediate the folding of chromatin fibers into radially oriented loops (8–10), a hierarchy of helical structures (11, 12), or an irregular network (13). Despite their disparities, all of these hypotheses assume that before higher-order compaction, the nucleosome chain forms a 30-nm chromatin fiber as the second level of DNA folding.

The concept of the 30-nm fiber in mitotic chromosomes is based on the following 2 observations: (*i*) fibers of ≈30 nm in diameter have been observed in chromosomes by conventional transmission electron microscopy (TEM) (14, 15); and (*ii*) X-ray scattering analysis of isolated mitotic chromosomes reveals a diffraction peak that is characteristic of a structure of 30-nm size (16, 17). However, in classical TEM studies, mitotic chromosomes were swollen in hypotonic buffers, and then chemically fixed, dehydrated with alcohol, and embedded into plastic (6, 7). These harsh nonphysiological treatments might have generated artificial de novo folding of chromatin. Also, X-ray scattering experiments have failed to provide unequivocal evidence that the 30-nm signal is derived from chromatin, rather than contaminating cytoplasmic material. Hence, these observations do not provide conclusive evidence for the existence of 30-nm chromatin fibers in chromosomes in vivo.

Cryo-EM of vitreous sections has made it possible to overcome the limitations of the methods described above (18). Cryo-EM is based on vitrification of the water by rapid cooling, which ensures immobilization of all of the macromolecules in the specimen in a close-to-native state (19). Thin vitrified samples, such as layers of macromolecule suspensions, are then directly observed under a cryo-EM without any chemical fixation or staining (19). Bulky samples, like the majority of eukaryotic cells or tissues, must be cut into thin vitreous sections before observation (18). This approach enables a direct high-resolution imaging of cell structures at close-to-native state. However, the interpretation of cryo-EM images is hampered by the effects of the contrast transfer function (CTF), which may cause certain structural features to be artificially amplified or suppressed (20).

Although 30-nm chromatin fibers can be routinely observed by cryo-EM in chromatin suspensions in vitro (21, 22), cryo-EM studies of HeLa S3 cells did not reveal this structural feature in mitotic chromosomes (23). Nevertheless, because the influence of the CTF was not compensated for, it remained unclear whether the absence of 30-nm fibers in cryo-EM images of mitotic chromosomes is characteristic of the native chromatin or an artifact of the imaging properties.

In the present study, we address this uncertainty by analyzing the CTF-corrected cryo-EM images of vitreous sections of human mitotic chromosomes in situ after isolation. We show that within the bulk of the mitotic chromosome, the chromatin fiber exists in a highly disordered and interdigitated state, comparable with a polymer melt. We will also demonstrate that chromosome swelling by reduction of Mg^{2+} concentration in the buffer results

Author contributions: M.E., K.M., and J.D. designed research; M.E., K.M.M., and K.M. performed research; K.M.M. and K.M. contributed new reagents/analytic tools; M.E., K.M.M., and A.S.F. analyzed data; and M.E., K.M.M., K.M., A.S.F., and J.D. wrote the paper.

The authors declare no conflict of interest.

[1]M.E., K.M.M, and K.M. contributed equally to this work.

[2]To whom correspondence should be addressed. E-mail: eltsov@embl.de.

This article contains supporting information online at www.pnas.org/cgi/content/full/0810057105/DCSupplemental.